Ponderomotive snowplow electron acceleration with high energy tilted ultrafast laser pulses

Patrick Hunt

phunt@mines.edu

Colorado School of Mines

Alex Wilhelm

Colorado School of Mines

Daniel Adams

Colorado School of Mines

Shoujun Wang

Colorado State University

Reed Hollinger

Colorado State University https://orcid.org/0000-0003-1955-8840

Ze'ev Shpilman

Colorado Sate University https://orcid.org/0000-0003-0549-9683

Sina Anaraki

Colorado State University

Nathaniel Westlake

Colorado School of Mines

David Schmidt

Colorado School of Mines https://orcid.org/0000-0002-9091-8071

Jorge Rocca

Colorado State University https://orcid.org/0000-0002-8349-6907

Charles Durfee

Colorado School of Mines

Article

Keywords: Ponderomotive potential, particle acceleration, ultrafast pulses, spatial chirp, spatio-temporal shaping

Posted Date: April 3rd, 2024

DOI: https://doi.org/10.21203/rs.3.rs-4177060/v1

Additional Declarations: There is **NO** Competing Interest.

Ponderomotive snowplow electron acceleration with high energy tilted ultrafast laser pulses

Patrick Hunt[1*†], Alex Wilhelm[1†], Daniel Adams[1], Shoujun Wang[2], Reed Hollinger[2], Ze'ev Shpilman[2,4], Sina Anaraki[2], Nathaniel Westlake[1], David D. Schmidt[1], Jorge J. Rocca[2,3], Charles G. Durfee[1*]

[1*]Dept. of Physics, Colorado School of Mines, 1500 Illinois Street, Golden, 80401, CO, USA.
[2]Dept of Electrical & Computer Engineering, Colorado State University, 400 Isotope Dr, Fort Collins, 80521, CO, USA.
[3]Dept. of Physics, Colorado State University, 400 Isotope Dr, Fort Collins, 80521, CO, USA.
[4]Plasma Physics Department, Soreq NRC,81800, Yavne, Israel.

*Corresponding author(s). E-mail(s): phunt@mines.edu; cdurfee@mines.edu;
Contributing authors: awilhelm@mines.edu; daadams@mines.edu; Shoujun.Wang@colostate.edu; Reed.Hollinger@colostate.edu; zeevs@soreq.gov.il; Sina.Anaraki@colostate.edu; nathanielwestlake@mines.edu; daschmid@mines.edu; Jorge.Rocca@colostate.edu;
†These authors contributed equally to this work.

Abstract

The application of high intensity ultrafast lasers to compact plasma-based electron accelerators has recently been an extremely active area of research. Here, for the first time, we show experimentally that carefully sculpting an intense ultrafast pulse in the spatio-temporal domain allows ponderomotive pressure to be used for *direct* acceleration of electron bunches from rest to relativistic energies. With subluminal group velocity and above-threshold intensity, a laser pulse can capture and accelerate electrons, pushing on them like a snowplow. However, to accelerate electrons from rest, thegroup velocity much be reduced substantially: In this demonstration experiment, we achieve a group velocity of $\sim \mathbf{0.6}\boldsymbol{c}$

in a tilted pulse by focusing the output of a novel asymmetric pulse compressor we developed for the petawatt-class ALEPH system at Colorado State University. The output beam is in good agreement with our modeling, supporting our theoretical prediction that this direct laser-electron approach can exploit optical spatio-temporal control techniques to sculpt desired properties of electron beams, such as narrow energy and angular distributions. The tilted-pulse snowplow technique can be scaled from small-scale to facility-scale amplifiers to produce short electron bunches in the 10 keV−10 MeV range for applications including ultrafast electron diffraction and efficient injection into laser wakefield accelerators for acceleration beyond the GeV level.

Keywords: Ponderomotive potential, particle acceleration, ultrafast pulses, spatial chirp, spatio-temporal shaping

1 Main

Particle accelerators have led to some of the most important discoveries in fundamental physics [1–6] and practical applications [7–10]. The cost and physical scale of particle accelerators has motivated research into laser-based alternatives, focusing on accelerating low-mass electrons. One mechanism to apply pressure on electrons with laser pulses is the ponderomotive force, which pushes electrons away from regions of high laser intensity. As a cycle-averaged force, it is phase-insensitive, independent of the orientation of linear polarization, and the speed of the interaction depends on the group velocity. It is the dominant mechanism for setting up the space charge distribution in the laser wakefield accelerator (LWFA), first proposed by Tajima and Dawson [11] and demonstrated by a number of groups [12–14]. Accelerating electrons more directly by the laser beam without reliance on plasma effects has drawn much interest using several approaches (though the mechanisms listed here can be blended [15]). Many previous proposals and demonstrations are phase-sensitive: for example, excess kinetic energy resulting from tunneling ionization of high-charge ions can seed subsequent ponderomotive acceleration out of the focal spot [16, 17]; a beam can be structured to have a longitudinal electric field [18–21]; electrons can be injected at an angle into a Gaussian beam focus [22], and the nonlinear ($\vec{v} \times \vec{B}$) Lorentz force can be exploited for acceleration [18, 23–25].

To capture and accelerate electrons, the potential must move at a speed less than the speed of light (c). Since the ponderomotive force involves the gradient of the pulse envelope, group velocity (v_g) control techniques can be used to produce subluminal pulses. Group velocity control has been proposed using waveguide modal dispersion [26] and plasma refractive dispersion (e.g. [27, 28]). These approaches offer limited group velocity control; moreover the latter approaches can require large plasma densities that lead to large space charge effects [29]. In contrast, the group velocity can be controlled over a much wider range with spatio-temporal shaping. In recent years, there has been much interest in the optics community in spatio-temporal group velocity control [30–32]. Our group has worked with tilted pulses [33–35] and proposed using tilted pulses to control the interaction group velocity for ponderomotive acceleration

[36]. A 'flying focus' approach to ponderomotive acceleration, where a radial grating provides group velocity control through angular spectral dispersion in a Bessel focus, has also been proposed by Ramsey et al. [37]. This focusing technique has recently been used for traveling-wave pumping of an X-ray laser [38, 39].

The present work is, to our knowledge, the first experimental demonstration of capture and acceleration of electrons from rest using the ponderomotive force. Fig. 1 shows a graphical representation of our acceleration scheme. A beam with angular spectral dispersion (angular spatial chirp) is focused onto a gas jet created by flowing gas through a capillary tube. The angular chirp results in a tilted pulse front that slows the speed of the interaction between the pulse and the electrons. This slower group velocity of the intensity envelope allows the electrons to be captured and accelerated directly by the ponderomotive force. The resulting beam travels away from the driving laser beam direction, pushed to the side by the tilted pulse front.

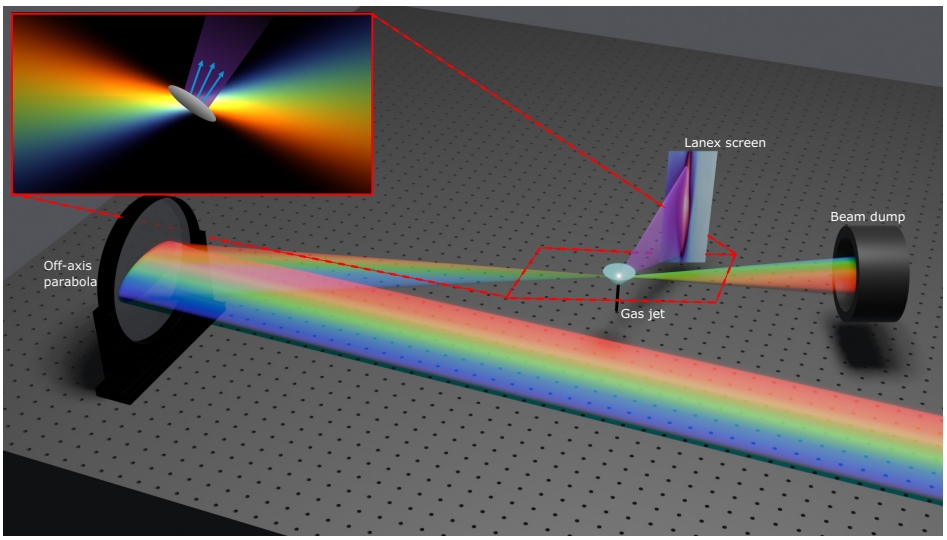

Fig. 1 A graphical representation of our acceleration scheme using a tilted pulse front. A propagating (right to left) spatially chirped laser pulse is focused with an off-axis parabola (left) which generates angular chirp resulting in pulse front tilt (as depicted by the gray ovoid in the inset image). The focus is located over a gas jet setup where the capillary is depicted by the vertical cylinder below the focus and the vertically oriented cone is the gas from the capillary. As the pulse passes through the focus, it ionizes the gas and accelerates the free electrons in a direction normal to the pulse front tilt (depicted by the magenta cones and arrows). The accelerated electrons are detected by observing fluorescence they induce on a Lanex screen, shown here with an actual measurement from our campaign in a pseudocolor map.

While the scheme can be scaled to lower-energy systems, for this proof-of-principle experiment we chose to utilize the beam from a large-scale laser facility to maximize the detectable signal. We find that the electrons are accelerated in the expected direction with output electron energies of up to 500 keV. It is a major technical advance to implement spatio-temporal engineering to produce a strongly tilted pulse at such a large scale. The confirmation of this self-injecting scheme points the way to using

beam shaping to produce electrons with better emittance and lower energy spread than demonstrated here.

As illustrated in Fig. 2a, the output energy can be varied from 10's of keV to >10 MeV by varying the pulse front tilt along with the focused intensity. For large pulse front tilt, the scheme can be implemented on amplifiers of only several mJ. Since the ponderomotive force is inversely proportional to the relativistic mass[40], the optimum application space for ponderomotive schemes is for modest energy ($< 1-10$ MeV). This energy range is complementary to wakefield schemes that can achieve higher energy but still require injection of energetic electrons. As a scheme that does not require the presence of a plasma, ponderomotive acceleration can be used to accelerate electrons (or even positrons [41]), with output beam characteristics that can be tailored by the properties of the laser beam. We anticipate this method can find applications for injection into other laser based accelerators such as LWFA or for ultrafast electron diffraction [42].

2 Single-particle theory of ponderomotive acceleration

The concept of controlling the group velocity to enable capture and acceleration using the cycle-averaged ponderomotive force was developed independently by several groups, including ours. Sazegari [27] and Mendonca [28] both proposed using the dispersion of the plasma to reduce the group velocity; Robinson [29] recently showed that this requires unrealistically high density. Spatio-temporal shaping [36, 37] provides for vacuum control over the group velocity. In our earlier paper [36], we developed a single-particle theory which was confirmed by a 2-dimensional particle-in-cell code. Here, we will summarize the theory behind ponderomotive acceleration with an emphasis on deriving scaling rules for practical implementation.

For *non-relativistic* motion of an electron (charge $-e$, mass m_e) driven in vacuum by a linearly polarized laser field (frequency ω, wavelength λ), the cycle averaged kinetic energy can be expressed in terms of the field amplitude (E_0), the intensity ($I_0 = \frac{1}{2}\epsilon_0 c E_0^2$), or the normalized vector potential ($a_0 = eA_0/m_e c$):

$$U_p = \frac{e^2 E_0^2}{4 m_e \omega^2} = \frac{r_e \lambda^2}{2\pi c} I_0 = m_e c^2 \frac{a_0^2}{4}. \tag{1}$$

In the second form, r_e is the classical electron radius. Mora et al. [43] calculated the total relativistic energy of the electron in the laser field as $\mathcal{E} = \bar{\gamma} m_e c^2$ where the relativistic factor using the cycle-averaged kinetic momentum $\bar{p}$ is :

$$\bar{\gamma} = \sqrt{1 + \frac{\bar{p}^2}{m_e^2 c^2} + \frac{2U_p}{m_e c^2}}. \tag{2}$$

From this energy, the force on the electrons is $-\frac{1}{\bar{\gamma}} \nabla U_p$. The $\bar{\gamma}^{-1}$ factor in front of the gradient term results in a decrease in the force experienced by the particle as the particle energy becomes more relativistic, as pointed out in earlier work [40]. Now consider a case where the local group velocity of the pulse front is moving at v_{pf},

with $v_{pf}/c = \beta_{pf} < c$. Under these conditions, it is possible for an electron initially at rest to be captured by this pulse front and accelerated. Treating this as a one-dimensional problem, the condition for electron capture and acceleration can be found using energetic considerations. Using a Lorentz transform to shift to a reference frame moving at the pulse front velocity (v_{pf}), the ponderomotive potential is stationary, and an electron (initially at rest in the lab frame) moves toward the potential with momentum $\boldsymbol{p} = -\gamma_{pf} m_e \boldsymbol{v}_{pf}$, with a relativistic correction factor of

$$\gamma_{pf} = \frac{1}{\sqrt{1-\beta_{pf}^2}}. \tag{3}$$

Provided that the potential height (U_{p0}) is sufficiently high, the electron trajectory will reverse at a position where the total energy of the electron on the potential is equal to the total initial energy. This defines the capture threshold,

$$U_p^{cap} = \frac{1}{2} m_e c^2 (\gamma_{pf}^2 - 1), \tag{4}$$

or in terms of the normalized vector potential, $a_{cap} = \sqrt{2}|\beta_{pf}|\gamma_{pf}$. In the simple non-relativistic limit, the capture threshold for the ponderomotive potential is simply equal to the classical kinetic energy $\frac{1}{2} m_e v_{pf}^2$; relativistically, the capture potential rises to infinity as $v_{pf} \to c$, the relativistic capture potential goes to infinity, showing that v_{pf} must be less than c. In this moving frame, when the capture condition is satisfied, the electron 'reflects' from the potential and leaves with a momentum of the opposite sign. Transforming back to the lab frame, we find that for this one-dimensional model, the maximum kinetic energy that a particle initially at rest can reach is $\mathcal{E}_{out} = 4U_p^{cap} = m_e c^2 a_{cap}^2$. Provided that $U_{p0} > U_p^{cap}$, the maximum energy depends only on the pulse front velocity and not on the pulse peak intensity. The upper panel of Fig. 2a shows how the capture potential (solid line) scales with the effective pulse front velocity. With group velocity control, the ideal maximum output energy (dashed) can be tuned.

We now turn to the question of group velocity control. Our novel approach is to employ tilted pulses that results from simultaneous spatial and temporal focusing (SSTF) [33–35, 44]. The spectral components of a pulse are spatially overlapped but the beam angle to the propagation axis is frequency-dependent,

$$\theta_x(\omega) = \Gamma(\omega - \omega_0), \tag{5}$$

(see Fig.1). In Supplementary Information section 1 (SI-1) we show that this angular dispersion results in a pulse front tilted at an angle to the propagation direction according to $\tan\theta_{pf} = \Gamma\omega_0$. The geometry of this tilted pulse, idealized to be infinitely wide, is shown in Fig. 2b, where it can be seen that tilt results in an effective pulse front velocity of $v_{pf} = c\cos\theta_{pf}$ (see SI-1). Now the capture condition can be written in terms of the pulse front angle by using Eqn. 3, $\gamma_{pf} = (\sin\theta_{pf})^{-1}$, and $U_p^{cap} = \frac{1}{2} m_e c^2 / \tan^2\theta_{pf}$.

The upper horizontal scale of Fig. 2a shows how the intensity required for capture and the maximum acceleration energy ($4U_p^{cap}$) scale with the pulse front tilt angle. The attractiveness of this scheme is evident: all electrons in the beam will be captured and accelerated in the same direction with the same energy. The tilted pulse produces a beam that is automatically separated from the driving laser beam, which is convenient for practical applications.

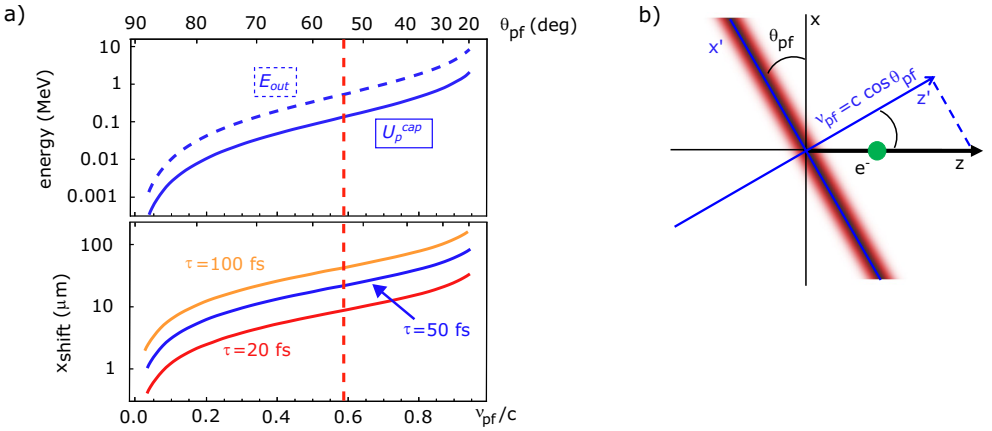

Fig. 2 (a) Log plots of the capture energy (upper, solid), ideal maximum output energy (upper, dashed) and the transverse shift (lower) during acceleration. The lower axis shows the dependence on the pulse front velocity (V_{pf}) relative to the speed of light; the upper horizontal axis shows the dependence on the pulse front tilt angle (θ_{pf}). In the lower panel, x_{shift} is calculated for the three pulse duration's shown. (b) Geometric diagram of infinitely wide beam concept shown as a red line with a fading gradient that is propagating along the (black) z axis, tilted by an amount (θ_{pf}), and traveling at the speed of light, c in the z-direction. During interaction with a stationary electron, green circle, the speed of the pulse is reduced to V_{pf}, and the electron is accelerated along the tilted (blue) z' axis. The vertical red line in both plots (a) represents the pulse front tilt achieved in this work.

The 3-dimensional effects of the finite-sized beam puts important constraints on the experimental design. The two most important aspects [36] are the connection between the acceleration time and the finite beam width and the curvature of the intensity contour in 3 dimensions. As the electrons are accelerated in the direction of the pulse front normal, the pulse moves behind them so that they interact with the trailing edge of the tilted pulse. The lower panel of Fig. 2a shows an analytic calculation of this transverse displacement (x_{shift}) during the acceleration process. This distance, which represents the minimum focal spot width required for electrons to be fully accelerated, was calculated for an infinitely wide tilted pulse that is triangular in temporal shape (see SI-2): $x(\Delta t) = 4c\tau_T/(R_{OT}\tan\theta_{pf})$, where $R_{OT} = U_{p0}/U_p^{cap}$. While it might seem that x_{shift} would decrease with θ_{pf} since the force is more forward-directed, in fact, the relativistic mass increase at large v_{pf} causes the electron to dwell longer on the pulse front during acceleration. The plot also demonstrates that short pulse durations are favorable, yielding high peak intensity and faster acceleration time, allowing the use of a smaller focal spot. For large θ_{pf} and short pulse duration, the 'reflection' of the electrons is faster, making the pulse front more closely resembling a ponderomotive

'mirror' for electrons [28]. The second consideration in the realistic application of ponderomotive acceleration is curvature of the pulse front. Variation of the transverse intensity profile leads to curvature in the contour at the threshold intensity value (illustrated in the inset of Fig. 1). For a Gaussian focal shape, this curvature is convex, leading to a diverging ponderomotive mirror shape.

3 Optical setup and experimental demonstration of ponderomotive snowplow acceleration

The laser source for our setup is the uncompressed fundamental ($\lambda_0 = 800$ nm) laser from the ALEPH petawatt-class laser facility at the Colorado State University (CSU) [45]. Referring to Fig. 3, the uncompressed pulse from the amplifier is reflected from a deformable mirror used for wavefront correction, then directed into our novel asymmetric four-grating compressor that delivers the spatially chirped pulses. An off-axis parabola focuses the beam to an effusive gas jet target.

The compressor (see Methods) was a key part of our experiment that we designed to deliver the spatially-chirped pulses. In previous work with smaller ($\sim$ 10 mm) beam diameters, we have developed compressors with variable output spatial chirp [46]. In this work with a much larger 55 mm beam size, we use a four-grating design with asymmetric distances between the two parallel grating pairs to deliver a beam with a fixed amount of transverse spatial chirp (see Fig. 3). The combined grating separation between the two pairs produces a compressed pulse at focus. A modest asymmetry was introduced in a four-grating pulse compressor recently [47] with the aim of smoothing the beam profile on the gratings. Other researchers have detuned the grating parallelism to introduce pulse front tilt, which leads to transverse chirp and a longer pulse at focus [48, 49]. Our approach allows for full bandwidth and transform-limited pulses at focus. For this proof-of-principle experiment, we arranged to maximize the spatial chirp exiting the compressor. Since the beam is spatially dispersed on all gratings except the first, the input energy is limited by the maximum fluence on the first grating at which it is safe to operate (70 mJ/cm^2). By choosing the first grating pair to be at a shorter grating separation, the aperture of the optics is reduced since the wavelengths cross between the last grating pair. Furthermore, since the beam is spatially chirped and not fully compressed after the first grating pair, the first pair can be in air, with the beam passing through a vacuum chamber window for gratings 3 and 4.

The chirped pulse is reflected from an $F/3$ ($f = 555$ mm) off-axis parabola which is focused at the approximate location of the tip of a continuous-flow gas jet. In contrast to alignment of a conventional compressor, where spatial chirp is undesirable, in our system it is imperative that the beamlets cross at the parabola focal plane, and that the individual beamlets are also well focused at the crossing plane. Provided that the gratings are parallel and the parabola is well aligned, the wavelength crossing will be at the focal plane. The beamlet focal plane and beam quality is then controlled by adjusting the input beam divergence and tuning out wavefront errors with the upstream deformable mirror.

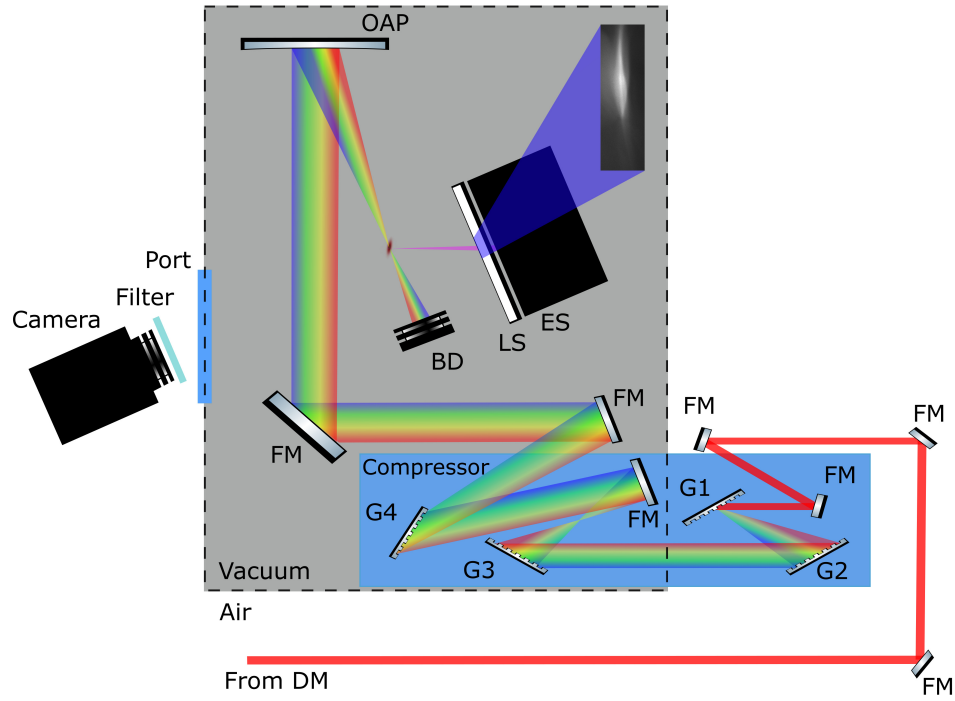

Fig. 3 Optical schematic from deformable mirror (DM) to focus of the pulse and electron acceleration measurement (magenta cone) with a Lanex screen (LS) and electron spectrometer (ES). The unbalanced four-grating compressor (shaded in blue) consists of four reflective gratings (G) with the first grating capable of translating parallel to the optical path allowing for tuning of the compression of the pulse at the focus. The second half of the compressor and acceleration is conducted in a high vacuum (10^{-6} Torr) chamber system (shaded in grey) while the first two gratings and folding mirrors (FM) up stream are in air. The spatially-chirped beam is focused with an off-axis parabola (OAP) then collected after focus with a beam dump (BD). The electron bunch generates a fluorescence pattern (a reference image from the campaign is shown) on the LS which is imaged by a camera outside of the chamber. The camera contains filters to block out laser light and is triggered by the laser system to capture the fluorescence from the corresponding shot.

To verify the spectral overlap and to locate the focus for placement of the jet target, a spectrally-resolved knife edge scan is performed [50]. Our analysis generates a ray trace of each spectral component of the chirped pulse as well as the location of the beam waist for each spectral component. Once the precise location of the focus is determined, a second harmonic crystal can be placed at the focus and a dispersion scan can be performed to optimize compression at the focus [51, 52]. During the campaign, a 34 μm spot size with a 90 fs duration with energy ranging from 750 mJ to 1.9 J was achieved, resulting in intensities from 2.39×10^{18} W/cm^2 to 6×10^{18} W/cm^2 and ponderomotive potentials of 143 keV to 362 keV.

A unique feature of this acceleration method is that the accelerated charge is nominally normal to the pulse front tilt and thus well-separated from the exiting laser pulse, as shown in Figs. 1 and 3, eliminating any need to use steering fields to separate the electron and laser beams. In previous work, small amounts of spatial chirp were used to deviate electrons from the driving laser beam in a LWFA scheme [49].

We placed a Lanex scintillating screen to the side of the beam that was normal to the leading side of the pulse front. This direction was calculated from the measured angular chirp as shown in Eqn. 5. The spectrally-resolved knife edge scan measurements yielded the angular dispersion, from which we calculated the pulse front tilt to be 54.6 ± 3.7^o. Fig. 4a shows the electron signal observed from a camera placed outside vacuum, using a cyclic pseudocolor map. Fig. 4b is an electron beam simulated from the calculated input laser conditions and using the published Lanex response curve [53] for the electron energy-dependent fluorescent efficiency. Overhead images of the setup were recorded to geometrically index the electron bunch trajectory, giving a measured electron beam direction of $68.78^o \pm 2.00^o$, which compares favorably with the 64^o direction calculated from the simulations. As predicted by simulation, the electron beam angular dispersion is narrower in the horizontal than in the vertical direction. This results from the shorter radius of curvature of the tilted pulse in the vertical direction.

Processed images of fluorescence were used to estimate electron bunch per shot with the use of a transfer function (Eqn. B15 in SI). For the data shown in Fig. 4a, the estimated electron yield for energies above 120 keV was 62.4 pC. A similar analysis from the image plate yielded approximately 2pC for the portion of the electron beam entering the spectrometer. In a separate measurement under different alignment conditions and a narrower field of view, we varied the input energy from 1.6 to 3.23 J, the yield ranged from 0.10 to 1.61 pC, demonstrating increased electron capture as more of the focal spot is brought above threshold for capture. We used a magnetic electron spectrometer with an image plate as the detector to measure the bunch energy. A developed image of the electron spectrum recorded during our campaign is shown in Fig. 4c with a calibrated energy plot directly below.

4 Discussion and outlook

To the best of our knowledge, this experiment is the first demonstration of ponderomotive capture and acceleration of electrons from rest. The electrons are emitted from the target with directions and energies that agree well with our model. The magnetic electron spectrometer measurements confirm that what is observed is an electron signal. Our calculations assume the plasma is ionized prior to acceleration; we estimate that the tunneling process preionizes the nitrogen gas to N^{5+} 50 fs prior to the arrival of the 4×10^{18} W/cm^2 peak intensity, well before the acceleration phase of the pulse (see SI-3). A topic of future exploration will be better establish the limits to the charge extraction efficiency for this approach. In principle, all electrons within the capture intensity contour are accelerated. The estimated yield of 62pC is substantially smaller than this prediction, and is likely limited by space-charge effects.

In light of these results, it is worth discussing extensions predicted by our model. First, we see that the shape of the intensity contour at the capture threshold plays a large role in the output beam divergence. The inset in Fig. 4b shows a calculation of the output beam using a super-Gaussian focal profile of the same spot area and pulse energy and a 55 fs pulse duration. As detailed in our earlier work [36], the flatter spatial intensity profile will lead to a dramatically narrower output beam divergence in both

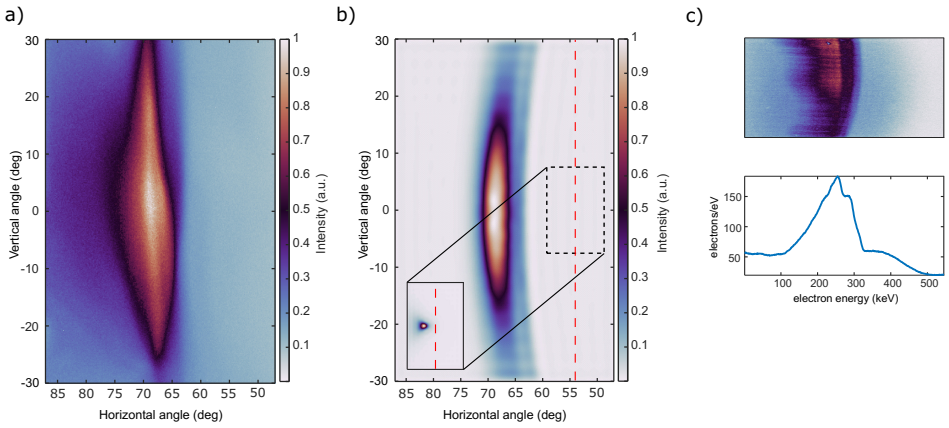

Fig. 4 (a) Image of measured electron intensity profile from Lanex screen, plotted in horizontal and vertical angular distribution, centered about the peak of the electron bunch intensity. The horizontal distribution is shifted to be centered around the geometrically measured pulse front tilt. (b) Simulated image of electron intensity profile from Lanex screen using geometric measurements of the pulse front tilt and Lanex response curve [53] with an inset of a simulation using a super-Gaussian profile and 55 fs pulse width. The dashed black rectangle indicates where the inset corresponds to the horizontal and vertical angle axis. Measured pulse front tilt is indicated by the dashed red vertical line at $\sim 54^o$. (c Upper) Developed image plate from electron spectrometer after 100 shots of laser system, plotted horizontally against electron energy. (c Lower) Cumulative energy plot of developed image plate. All intensity plots are plotted using a cyclic pseudocolor map.

directions. Second, shorter pulse duration also should result in a large improvement in the accelerated beam quality, since a faster acceleration time allows for complete acceleration with a smaller focal spot diameter. For example, with $\theta_{pf} = 17.7^o$, a 20 fs duration pulse with 520 mJ energy focused to a $3\,\mu$m $\times$ $26\,\mu$m spot size can accelerate electrons to 10 MeV. Finally, as noted in Ramsey et al. [37], if an accelerating group velocity can be designed to maintain high acceleration gradients during acceleration, even higher output energies can be reached. In the context of our tilted pulse approach, this can be achieved with a concave pulse front. Therefore, we anticipate that further beam engineering will enable this laser electron acceleration approach to find applications in ultrafast electron diffraction and as a seed for higher energy laser based accelerators.

Supplementary information. The Supplementary Information section provides details on the derivations of the effective pulse front velocity and the transverse motion along the pulse front as well as information about the alignment of the four-grating pulse compressor.

Acknowledgments. The CSM group gratefully acknowledges funding from the National Science Foundation (PHY-2206807) and beam time at the ALEPH laser awarded through LaserNetUS, under DOE Office of Science, Fusion Energy Sciences Contract No. DE- SC0021246. The CSU team acknowledges funding US Department of Energy, Fusion Energy Sciences IFE-STAR Program's RISE hub, and DoD Vannevar Bush Faculty Fellowship ONR award N000142012842.

Declarations

- Funding: see acknowledgements
- The authors have no conflict of interest or competing interests
- Ethics approval: Not applicable
- Consent to participate: Not applicable
- Consent for publication: Not applicable
- Data and code are available upon reasonable request.
- Authors' contributions: experimental concept PH, AW, CD; theory/modeling AW, CD; experimental design PH, AW, SW, RH, JR, CD; experimental alignment and operations PH, SW, SA, DS, DA, CD; pulse characterization PH, AW, DS, DA, CD; electron spectrometer ZS; data analysis PH, NW, ZS, CD; writing PH, CD.

Appendix A Methods

A.1 Chirped-pulse amplifier system

The laser source for our setup is the uncompressed fundamental ($\lambda_0 = 800$ nm) laser from the ALEPH petawatt laser facility at the Colorado State University (CSU). The system is capable of generating uncompressed pulses up to > 37 J per pulse [45], but to use the available 9×4 inch reflective gratings at a safe energy fluence, we used a beam that was 55 mm diameter with a flat-top profile, stretched to 550 ps at uncompressed energies up to 3 J per shot. The stretched pulse reflects from a deformable mirror used for wavefront correction, then directed into the asymmetric four-grating compressor, as depicted in Fig. 3 and described in the next section.

A.2 Spatial Chirp Compressor Design and Alignment

A.2.1 Compressor Design

The role of the asymmetric compressor is to deliver a beam that has transverse spatial chirp, so that when it is focused by the off-axis parabola, the pulse will be compressed as close as possible to the transform limit of the spectrum. The Supplementary section (SI-2) shows how the angular chirp rate determines the angle of the tilted pulse at the focus. The compressor is asymmetric in that the separations L_{12} and L_{34} between the two grating pairs is different, while their sum remains the same as in a conventional compressor. We note that it is advantageous to have $L_{34} > L_{12}$ to minimize the size of the beam on the gratings. Each grating pair is mounted in a parallel configuration. The first grating pair (G1, G2), nominally separated by $L_{12} = 31$ cm along the central wavelength λ_0 direction, is located outside of vacuum. G1 and its input mirror are mounted together on a translation stage that moves along the optical path towards G2. This allows the G1-G2 grating separation to be adjusted without changing the pointing of the output beam. Following G2, the collimated and spatially chirped beam is $\sim 63 \times 55$ mm and directed through a 16 mm thick window into a vacuum chamber (10^{-6} Torr) to the second half of the compressor grating pair. The second grating pair (G3, G4), nominally separated by 118 cm along λ_0, are mounted in vacuum to deliver the compressed pulse to the focusing parabola while avoiding nonlinear propagation

that would be introduced by a window. Following G4, the final collimated and spatially chirped beam is $\sim 77 \times 55$ mm. After exiting the compressor, the chirped pulse is directed onto an $F/3$ ($f = 555$ mm, 22^o turning angle) off-axis parabola which focuses the beam at the approximate location of the tip of a continuous-flow gas jet.

A.2.2 Compressor alignment

Our use of a strong spatial chirp at the output of the compressor adds complexity to the common challenges of grating compressor and off-axis parabola alignment for high-peak power chirped pulse amplifiers. In a conventional compressor, the gratings are aligned to be parallel, with a symmetric path between the two passes so as to eliminate spatial chirp. In a spatially-chirped beam, the propagation of each frequency component propagates independently from the rest. Ideally, each beamlet (the beam for a frequency component) should overlap at the focal plane of the parabola. Furthermore, the divergence of each beamlet should be collimated to place the focused beamlet at the wavelength crossing plane. The first component to be aligned is the deformable mirror. The deformable mirror was placed before the compressor, and was initially aligned by optimizing the wavefront of the uncompressed beam, based on leakage through a folding mirror viewed by a Shack-Hartmann wavefront sensor placed at the focus of a lens. Next, the grating pairs of the compressor are aligned. The grating pairs must be mounted parallel to each other and at an angle close to what is in the stretcher. A complete raytrace of the compressor aided in the physical placement of the gratings, then a collimated laser diode beam at 808 nm was used for the first alignment. The first grating pair is aligned by rotating the first grating to retroreflect the zeroth order of the incident beam back out through a pair of irises, allowing the the tip and tilt of the grating can be corrected as well. The grating is then rotated by the desired incident using the precision rotation stage mounted under the grating. The groove rotation around the grating normal is then set by ensuring the height of first order reflections matches the system beam height. Each subsequent grating is aligned in a similar manner. To increase the accuracy of the alignment of G1 and G2, a flat mirror is inserted to retroreflect an apertured broadband beam through those gratings, and the focus of the return beam is observed on a camera. This allows fine adjustments to be made to eliminate residual spatial chirp. The same procedure is used to refine the G3, G4 alignment. The final component to be aligned is the $F/3$ off-axis parabola. This was aligned by placing a high-resolution camera at the wavelength crossing plane and then stepped through focus as the degrees of freedom of the parabola are tuned. Once tuned, manual deformable mirror adjustments were used to optimize input beam divergence and the focal quality.

A.3 Knife Edge and Dispersion Scan

We employ a spectrally-resolved knife-edge scan [50] to validate successful wavelength alignment, determine the optimal focal position for jet target placement, and quantify the angular chirp, resulting in the calculation of the pulse front tilt angle. A knife edge is scanned transversely across the beam, while a fiber spectrometer measures the transmitted spectrum from an integrating sphere placed after the beam focus.

After making this measurement at several transverse planes along the optical axis, analysis yields a ray trace of each spectral component of the chirped pulse as well as the location of the beam waist for each spectral component. Once the precise location of the focus is determined, a second harmonic crystal can be placed at the focus and a dispersion scan can be performed to optimize compression of the pulse at the focus by varying the separation of the first grating pair [51, 52].

A.4 Gas jet target

The gas jet target consists of a metal capillary with a 132 μm inner diameter that provides a steady flow of nitrogen gas to the focus. A leak valve located upstream controls the backing pressure at the gas jet, which is monitored with a capacitance manometer. A calibration of the gas jet density was performed separately by imaging the fluorescence from varying gas pressure at a focused ultrafast pulse and comparing to the fluorescence generated by the pressure chamber back filled to a static pressure [54]. The gas jet, knife edges and nonlinear crystal are mounted to a 3-axis SmarAct linear stage assembly, allowing the gas jet to be located anywhere within the focus and path of the pulse.

A.5 Data Acquisition

Two methods were used to characterize the output charge. The first method was to place a scintillating screen (Lanex Fine) parallel to the driving laser beam on the side of focus in the direction of the expected acceleration. The Lanex screen was imaged by a camera placed outside vacuum. The camera was triggered by the laser system and filters were used to block laser light while still passing the fluorescence from the screen. Fig. 4a shows a representative image of the output beam. Images recorded the location of the screen with a calibration scale, allowing the angle of the output beam relative to the driving beam direction to be measured. While this measurement did not resolve the electron energies, the fluorescent yield of this type of scintillating screen as a function of electron energy has been reported by Glinec et al. [53]. The screen has an energy detection threshold of 120 keV, a peak at approximately 400 keV, and is constant above 2 MeV. As described in SI-4, we can use this response function along with optical collection efficiencies to estimate the quantity of accelerated electrons. The images of the Lanex screen were used to estimate a quantitative charge bunch and therefore need to have the photon yield of the screen isolated from the image. Reference images without the pulse were used to remove any background signal. The resulting image was then DC threshold yielding an estimate of the fluorescence.

The second measurement method utilized an in-house built and calibrated electron spectrometer [55]. To aid in locating the spectrometer entrance slit on the electron beam, a Lanex screen with an opening for the slit was placed in front of the spectrometer. The design of the spectrometer consists of magnetic plates mounted in a wedge configuration which generates a variable magnetic field and a detection range of $50 - 460$ keV. The detection screen for the spectrometer was an image plate, which must be removed from the spectrometer after the measurement and developed with a scanner. The detection range and sensitivity was simulated using SIMION and the

energy dispersion calibrated at the ALEPH facility by normalizing electron yield measurements with varying thicknesses of aluminum filters placed in front of the imaging plate. In our measurements, the electron signal was collected over 100 laser shots. The developed image plate was then scanned and analyzed for detected electrons.

A.6 Single-particle modeling

To predict the electron energy and angular distribution for electrons accelerated from the focal plane, we use the following simple form for the ponderomotive potential for the tilted pulse in the stationary lab frame:

$$U_p(x,y,z,t) = U_{p0} \exp\left(-2\frac{x^2+y^2}{w^2}\right) \exp\left(-\frac{2(ct - x\,\tan\theta_{pf} - (z-z_0))^2}{c^2\tau^2}\right), \quad \text{(A1)}$$

where the target plane is at $z = 0$, and the pulse starts at $z = z_0$ at t=0.

The relativistic equations of motion under the ponderomotive (or guiding-center) approximation can be calculated by associating the total energy of the particle with the Hamiltonian ($\mathcal{E} = \mathcal{H}$), and using the Hamiltonian equations of motion [43]:

$$\frac{d\bar{\boldsymbol{p}}}{dt} = -\frac{\partial \mathcal{H}}{\partial \boldsymbol{r}} = -\frac{1}{\overline{\gamma}}\nabla U_p \quad \text{(A2)}$$

$$\frac{d\boldsymbol{r}}{dt} = \frac{\partial \mathcal{H}}{\partial \bar{\boldsymbol{p}}} = -\frac{\bar{\boldsymbol{p}}}{\overline{\gamma} m_e} \quad \text{(A3)}$$

The derivatives for the force vector are evaluated symbolically and the set of equations are solved numerically for the trajectories. The output directions and kinetic energies are calculated from the final momentum vectors, allowing a geometric calculation of the position on the measurement screen. The electrons that are accelerated to within the region that is experimentally measured with our camera are accumulated into an array. Fig. 4b shows the predicted signal after applying the Lanex sensitivity function described above.

Appendix B Supplementary Information

B.1 SI-1: Tilted pulse front calculations

We use angular dispersion to produce a tilted pulse front. A framework to understand the formation of tilted pulses in the context of Gaussian beams was detailed in some papers from our group [33–35]. For a pulse traveling in the z-direction through the $z = 0$ plane, pulse front tilt means that the pulse arrival time (group delay) varies linearly with the transverse position (x). Control of the spatio-temporal intensity profile in our scheme involves exploiting the properties of pulses with spatial chirp, that is, where the frequency components of the beam have a frequency-dependent direction (angular chirp) and transverse offset (transverse chirp), as depicted in Fig. 1. In the simplest formulation, consider a set of plane waves traveling with wave vectors in the x-z plane

with direction that varies linearly with frequency (angular chirp):

$$E(x,y,z,t) = E_0(\omega)\exp\left[i\frac{\omega}{c}(x\sin\theta_x + z\cos\theta_x) - i\omega t\right], \tag{B4}$$

where the angular spread is in the x-z plane with an angle, $\theta_x(\omega)$, to the z-axis. Here, $E_0(\omega)$ is the spectral amplitude and we parameterize the angular chirp as $\sin\theta_x = (\omega-\omega_0)\Gamma$. Evaluating the field at z=0, the spectral phase of the wave is $\phi(\omega,x) = x\Gamma\omega(\omega-\omega_0)/c$. The arrival time of the pulse is calculated by evaluating the group delay

$$\partial_\omega\phi(\omega,x)|_{\omega_0} = x\Gamma\omega_0/c. \tag{B5}$$

We see this varies linearly with the transverse position, which shows that the pulse front is tilted. Defining a pulse front tilt angle, (θ_{pf}), so that $\theta_{pf} = 0$ for a pulse front perpendicular to the direction of beam propagation, we find that

$$\tan\theta_{pf} = \Gamma\omega_0. \tag{B6}$$

This construction describes a pulse front that is tilted relative to the propagation direction of the central frequency of the pulse spectrum and is infinitely wide. It is this form that is used in our analytic work later in this section. Pulse front tilt can also result from a combination of transverse chirp and overall spectral phase [56], or in general, a combination of angular and transverse chirp. The advantage of working with pure angular chirp is that the full bandwidth is present where the frequency components of the beam overlap, allowing the pulse to reach its minimum possible pulse duration. Otherwise, the reduction in the local bandwidth will decrease the local peak intensity [35, 44].

To model a finite beam size [35], we treat each frequency component as a Gaussian beam that enters the focusing element with a frequency-dependent transverse displacement $x_s(\omega) = (\omega-\omega_0)\alpha$. The focusing optic (a lens or off-axis parabola) converts this transverse chirp into an angular chirp so that $\Gamma = -\alpha/f$, where f is the focal length. Each Gaussian beam focuses to a waist at the focal plane and is ideally overlapped there. Therefore, with good optics and careful alignment, the beam reaches a diffraction-limited spot size and a transform-limited pulse duration.

We can use the time-domain intensity profile for the idealized tilted pulse that has a uniform transverse intensity profile since the mathematics can be solved more easily than for a finite beam size. In this case, the distribution of the ponderomotive potential can be written as

$$U_p(x,z,t) = U_{p0}\,exp\left[-\frac{2(c\,t - x\,\tan\theta_{pf} - z)^2}{c^2\tau^2}\right], \tag{B7}$$

where τ is the transform-limited pulse duration. We can then transform to an $\{x', z'\}$ coordinate system aligned with the pulse front, so that the force exerted on the electron

is along the pulse front normal (z') as shown. Rotating the coordinate system, so that

$$U_p(z',t) = U_{p0}\, exp\left[-\frac{2(c\,\cos\theta_{pf} - z')^2}{(c\,\cos\theta_{pf})^2\tau^2}\right], \tag{B8}$$

it can be seen that the pulse front moves slower than c: $v_{pf} = c\cos\theta_{pf}$ and that there is no dependence on the x' coordinate. For our theoretical calculations, we use this form of the tilted pulse, evaluated at the focal plane. We can also express the time-domain field as a function of position within the focus. For wider bandwidths and tighter focusing, it becomes important to use the more complete representation of the intensity, but for our conditions we found little departure from the simpler form.

B.2 SI-2: Calculation of transverse motion during acceleration

As discussed in the main text, electrons being accelerated will move in the transverse direction during the acceleration process. Designating this transverse motion (x_{shift}), the focal spot diameter must be greater than this distance for the electrons to reach their full energy. For example, if the spot diameter is equal to $2x_{shift}$, then electrons starting in half of the focal region would be expected to reach full energy. As in the previous section, we first rotate the coordinate system to axes aligned with the pulse front, then we boost to a reference frame moving with the pulse $\{c\,t'', x'', 0, z''\}$ so that the potential is stationary. For the Gaussian temporal pulse shape, the potential in the rotated moving frame is

$$U_p(z'',t) = U_{p0}\, exp\left[-\frac{2z''^2}{\gamma_{pf}^2 c^2\cos^2\theta_{pf}\tau^2}\right] = U_{p0}\, exp\left[-\frac{2z''^2\,\tan^2\theta_{pf}}{c^2\tau^2}\right], \tag{B9}$$

where the last form makes use of $\gamma_{pf} = 1/\sin\theta_{pf}$.

While the equations of motion can be solved for the Gaussian potential, a simpler closed-form solution can be obtained by treating the temporal pulse shape as triangular, resulting in a constant gradient of the potential. In the rotated, moving reference frame, the total energy of the electron, $\mathcal{E} = \overline{\gamma} m_e c^2$, is conserved, leading to the conclusion that $\overline{\gamma} = \gamma_{pf}$. This simplifies the solutions to the trajectory, using Eqns. A2 and A3. The acceleration is only in the z'' direction, with the trajectory

$$z''(t'') = \frac{U_{p0}}{2m_e\gamma_{pf}^3 v_{pf}\tau_T}t''^2 - v_{pf}t'', \tag{B10}$$

where τ_T is the pulse half width from the peak to where it reaches zero, and we have assumed the electron starts at rest (in the lab frame) at the origin. In the moving frame, the electron moves up the potential and reverses direction, so that when it returns to the origin, it is a free particle moving in the $+z''$ direction. The time (in the moving frame) spent on the potential $\Delta t''$ can be found by setting Eqn. B10 to

zero, resulting in,

$$\Delta t'' = \frac{2m_e v_{pf}^2}{U_{p0}} \gamma_{pf}^3 \tau_T. \tag{B11}$$

Performing a Lorentz transform back to the lab frame adds an additional factor of γ_{pf}, resulting in,

$$\Delta t \propto \frac{4}{R_{OT}} \gamma_{pf}^2 \tau_T, \tag{B12}$$

where $R_{OT} = U_{p0}/U_p^{cap}$ is the ratio by which the focused intensity exceeds the capture potential. During the acceleration time, (Δt), the electron will shift in the transverse direction by

$$x(\Delta t) = \frac{4c\tau_T}{R_{OT} \tan\theta_{pf}}. \tag{B13}$$

This calculation indicates that more electrons will experience the full acceleration as the pulse duration decreases and/or the focal spot width increases along the axis of the spatial chirp. Some examples are illustrated in Fig. B1. In Fig.B1a, we simulate the image on the Lanex screen for a pulse with the same energy but 50 fs in duration. The calculated shape of the output electron beam profile is not strongly dependent on the pulse duration, but we do see somewhat more signal at smaller deflection angles. Fig. B1b shows a calculation of the screen position as a function of the starting transverse position in the focal plane. Comparing the blue line (for 90 fs pulse duration) with the dotted green line (for 50 fs, same laser energy), we see that the shorter pulse brings more of the focal spot above laser energy, and that those additional electrons have a longer effective acceleration length than those that start closer to the center of the focal spot.

Fig. B1b also illustrates the role of the pulse duration as the peak intensity is held constant (solid lines). The effect is the most dramatic for the shorter pulse duration, where the electrons are directed closer to the pulse front normal. Fig. B1c shows the correlation of the output energy to the output angle, as well as the relative yield distribution. Shorter pulses allow more of the electrons to approach the ideal maximum energy, which for these conditions is 1 MeV.

A related issue is the initial state of the electrons prior to acceleration. The gas target was molecular nitrogen, which undergoes tunneling ionization early in the temporal profile of the pulse.

B.3 SI-3: Estimate of electron yield

Although a direct measurement for beam charge was not available, we can estimate the electron yield from the fluorescent emission measured with the external CCD camera. The Lanex photon yield [53],

$$\frac{d\gamma_{cr}}{dn_{inc}} = \left(\frac{1}{E_{ph}}\right) \epsilon \left(\frac{dE}{dx}\right) \left(\frac{h_s}{\rho_{GS} \cos\theta_\perp}\right) \zeta = \left(\frac{1}{E_{ph}}\right) \epsilon \left(\frac{dE}{dx}\right) \delta x\, \zeta \tag{B14}$$

consists of a photon energy of $E_{ph} = 2.27$ eV emitted at 546 nm, an intrinsic efficiency of $\epsilon = 16\%$, kinetic yield energy of $dE/dx = 11.25$ MeV/cm, an equivalent

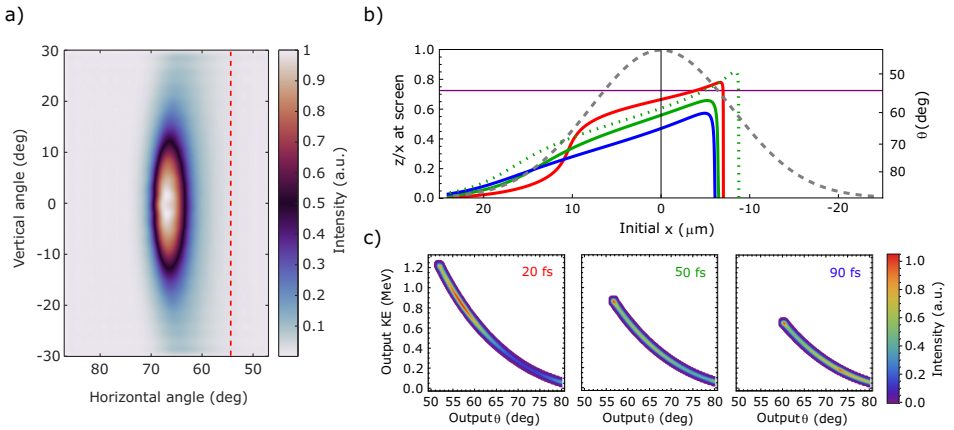

Fig. B1 (a) Simulated image of signal on the Lanex screen for the same conditions as in Fig. 4, but for a pulse duration of 50 fs. The pulse front tilt is indicated by the vertical dashed red line. (b) Calculation of the output direction of the electrons as a function of the starting position in the focal plane for different pulse conditions. The sign of the position is consistent with Fig. 2b, where the leading edge of the tilted pulse is at negative position relative to the optical axis. The solid lines correspond to a constant peak intensity as the pulse duration is varied. The dotted line corresponds to a 50 fs pulse duration with the same energy as the 90 fs case. (c) Calculation of the correlation of the output kinetic energy with the direction of the electrons. The color scale represents the relative yield for each of the cases.

thickness of pure gadolinium oxysulfide (GOS) of $\delta x = h_s/\rho_{GS}\cos\theta_\perp = 4.758\,\mu$m given an incident electron trajectory of $\theta_\perp = 21.22^o$ (relative to normal of Lanex screen), a 6x low energy enhancement factor, and a transmission output factor of $\zeta = 22\%$. When combined with a normalized Lambertian distribution with the camera parallel ($\theta_{CCD} = 0^o$) to the Lanex screen, a collection solid angle of $\Omega = 0.44$ msr, transmission through three lenses (99%) and two BG39 filters (77%), and the parameters of the camera, $QE = 60\%$ with 23 ke^- well-depth at 16-bit depth, the incident electron bunch can be estimated from the measured signal of de-noised images of the Lanex screen,

$$\left(\frac{d\gamma_{cr}}{dn_{inc}}\right)\left(\frac{\cos\,\theta_{CCD}}{\pi}\right)\Omega\,Tx_{lens}^3\,Tx_{BG39}^2\,QE\left(\frac{ADC}{e^-}\right) = \frac{dn_{cts}}{dn_{inc}}. \tag{B15}$$

B.4 SI-4: Analysis of Spectrally-Resolved Knife Edge Scans

Data from the spectrally-resolved knife edge scan (See Methods) is analyzed which yields parameters of the full SSTF beam, particularly the average angular chirp (pulse front tilt). Raw spectrometer data from the scan is denoised and estimated beam parameters (beam waist and Rayleigh length) are calculated from inputs regarding the setup to be used as initial guesses. With the spectrometer data denoised, a subset of spectral components across the spectrum of the pulse are sampled. At each z position along the optical axis, the sampled spectral data (intensity) as a function of x is fit to an error function,

$$I_k(x) = I_0 \frac{1}{2}\left(1 - \mathrm{erf}\left(\frac{\sqrt{2}(x_k - x_0)}{w_l}\right)\right), \tag{B16}$$

where I_0 is the overall intensity, x_0 is the half-power position, and w_l is the beamlet radius ($1/e^2$) for the k^{th} spectral component. With the x-z position and a known beamlet radius for the spectral components determined, a ray trace for each spectral component is calculated with a linear regression, as shown in Fig. B2.

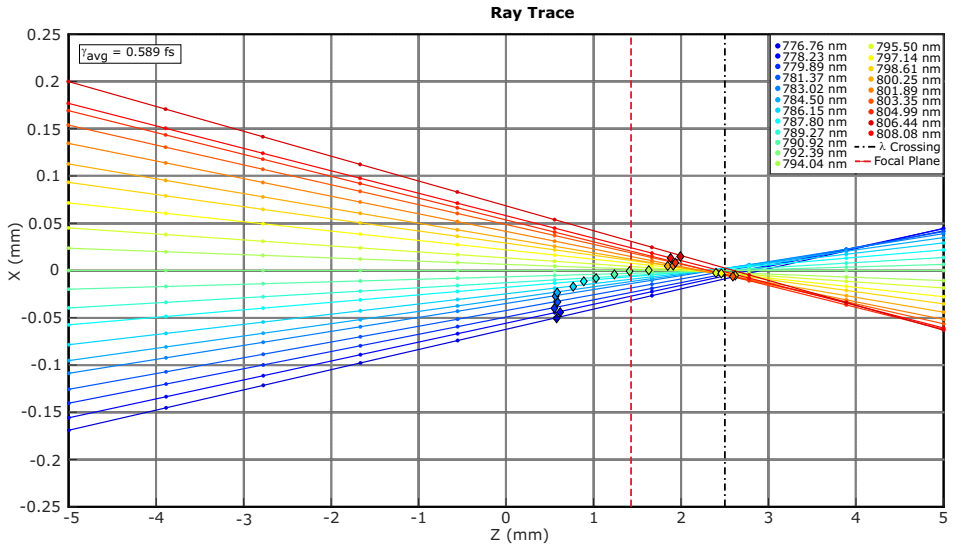

Fig. B2 Ray trace generated from analyzed data of knife edge scan during our campaign at CSU mapped out on a plane defined by the optical axis (z) and the horizontal transverse (x) distance. The sampled spectral components are traced in their corresponding colors from the fitted x-z points (indicated by filled circles). The average wavelength crossing is marked by a black dashed line. The beamlet focal spots are marked by colored diamonds and yield the average focal plane, marked by a red dashed line. The difference in plane locations is likely due to chromatic aberrations in the beam, as indicated by the pattern of the spectral focal positions.

With this set of rays across the spectrum, the wavelength crossing plane can be determined. The angular dispersion is also calculated, leading directly to the calculated pulse front tilt (See SI-1). In order to determine the focal spot size and position for each spectral component, the beamlet radii as a function of z position is fit to the following function,

$$w(z) = w_0 \sqrt{1 + \left(M^2 \left(\frac{z - z_0}{z_R}\right)\right)^2}, \tag{B17}$$

where w_0 is the beamlet waist, M^2 is the beamlet m-squared value, z_0 is the beamlet waist position, and z_R is the beamlet Rayleigh range. The average beamlet focal plane can then be calculated and compared to the wavelength crossing plane. Comparing the two planes as well as the pattern of the focal planes allows one to determine the

quality of the beam as well as placement for the second harmonic crystal (Dispersion Scan) and the gas jet. For our measurement during the campaign (Fig. B2), it can be seen that there is some chromatic variation in the focal distance that results from cumulative effects through the long amplifier chain. While there is an offset in the wavelength crossing and the average beamlet focal plane, our analytic calculations indicate that as long as the target is placed where the spectral components cross, the pulse front tilt and shape is not greatly affected by the beamlet divergence.

References

[1] Hofstadter, R.: Structure of Nuclei and Nucleo Extension of electron-scattering studies to hil energies gives a new model of the neutron and pro (1962). https://www.science.org

[2] Breidenbach, M., Friedman, J.I., Kendall, H.W., Bloom, E.D., Coward, D.H., Destaebler, H., Drees, J., Mo, L.W., Taylor, R.E.: OBSERVED BEHAVIOR OF HIGHLY INELASTIC ELECTRON-PROTON SCATTERING (1969)

[3] Friedman, J.I., Kendall, H.W.: Deep inelastic electron scattering. Annual Review of Nuclear Science **22**(1), 203–254 (1972)

[4] Aad, G., Abajyan, T., B. Abbott, e.a.: Observation of a new particle in the search for the standard model higgs boson with the atlas detector at the lhc. Physics Letters, Section B: Nuclear, Elementary Particle and High-Energy Physics **716**, 1–29 (2012) https://doi.org/10.1016/j.physletb.2012.08.020

[5] Chatrchyan, S., Khachatryan, V., al., A.M.S.: Observation of a new boson at a mass of 125 gev with the cms experiment at the lhc. Physics Letters, Section B: Nuclear, Elementary Particle and High-Energy Physics **716**, 30–61 (2012) https://doi.org/10.1016/j.physletb.2012.08.021

[6] Foka, P., Janik, M.A.: An overview of experimental results from ultra-relativistic heavy-ion collisions at the CERN LHC: Bulk properties and dynamical evolution. Elsevier B.V. (2016). https://doi.org/10.1016/j.revip.2016.11.002

[7] Landis, G.A., Armini, A.J., Greenwald, A.C., Kiesling, R.A.: Apparatus and technique for pulsed electron beam annealing for solar cell production. In: 15th Photovoltaic Specialists Conference, pp. 976–980 (1981)

[8] Thomae, R.: Recent developments in ion implantation accelerators. Nuclear Instruments and Methods in Physics Research Section B: Beam Interactions with Materials and Atoms **50**(1-4), 444–454 (1990)

[9] Blackmore, E.W., Evans, B., Mouat, M.: Operation of the triumf proton therapy facility. In: Proceedings of the 1997 Particle Accelerator Conference (Cat. No.97CH36167), vol. 3, pp. 3831–38333 (1997). https://doi.org/10.1109/PAC.1997.753430

[10] Chen, G., Bjorkholm, P., Fox, T.R., Wilson, Z., Bonsergent, X.: X-Ray Cargo Inspection: Status and Trends. AIP Conference Proceedings **1099**(1), 570–573 (2009) https://doi.org/10.1063/1.3120101 https://pubs.aip.org/aip/acp/article-pdf/1099/1/570/11509382/570_1_online.pdf

[11] Tajima, T., Dawson, J.M.: Laser electron accelerator. Physical Review Letters **43**(4), 267–270 (1979) https://doi.org/10.1103/physrevlett.43.267

[12] Modena, A., Najmudin, Z., Dangor, A.E., Clayton, C.E., Marsh, K.A., Joshi, C., Malka, V., Darrow, C.B., Danson, C., Neely, D., Walsh, F.N.: Electron acceleration from the breaking of relativistic plasma waves. Nature **377**(6550), 606–608 (1995) https://doi.org/10.1038/377606a0

[13] Malka, V., Fritzler, S., Lefebvre, E., Aleonard, M.-M., Burgy, F., Chambaret, J.-P., Chemin, J.-F., Krushelnick, K., Malka, G., Mangles, S.P.D., Najmudin, Z., Pittman, M., Rousseau, J.-P., Scheurer, J.-N., Walton, B., Dangor, A.E.: Electron Acceleration by a Wake Field Forced by an Intense Ultrashort Laser Pulse. Science **298**(5598), 1596–1600 (2002) https://doi.org/10.1126/science.1076782

[14] Tajima, T., Yan, X.Q., Ebisuzaki, T.: Wakefield acceleration. Reviews of Modern Plasma Physics **4**(1), 7 (2020) https://doi.org/10.1007/s41614-020-0043-z

[15] Hegelich, B.M., Labun, L., Labun, O.Z.: Revisiting Experimental Signatures of the Ponderomotive Force. Photonics **10**(2), 226 (2023) https://doi.org/10.3390/photonics10020226

[16] Moore, C.I., Ting, A., McNaught, S.J., Qiu, J., Burris, H.R., Sprangle, P.: A Laser-Accelerator Injector Based on Laser Ionization and Ponderomotive Acceleration of Electrons. Physical Review Letters **82**(8), 1688–1691 (1999) https://doi.org/10.1103/physrevlett.82.1688

[17] Moore, C.I., Ting, A., Jones, T., Briscoe, E., Hafizi, B., Hubbard, R.F., Sprangle, P.: Measurements of energetic electrons from the high-intensity laser ionization of gases. Physics of Plasmas **8**(5), 2481–2487 (2001) https://doi.org/10.1063/1.1347033

[18] Kimura, W.D., Kim, G.H., Romea, R.D., Steinhauer, L.C., Pogorelsky, I.V., Kusche, K.P., Fernow, R.C., Wang, X., Liu, Y.: Laser Acceleration of Relativistic Electrons Using the Inverse Cherenkov Effect. Physical Review Letters **74**(4), 546–549 (1995) https://doi.org/10.1103/physrevlett.74.546

[19] Wootton, K.P., Wu, Z., Cowan, B.M., Hanuka, A., Makasyuk, I.V., Peralta, E.A., Soong, K., Byer, R.L., England, R.J.: Demonstration of acceleration of relativistic electrons at a dielectric microstructure using femtosecond laser pulses. Optics Letters **41**, 2696 (2016) https://doi.org/10.1364/ol.41.002696

[20] Palastro, J.P., Antonsen, T.M., Morshed, S., York, A.G., Milchberg, H.M.: Pulse

propagation and electron acceleration in a corrugated plasma channel. Phys. Rev. E **77**, 036405 (2008) https://doi.org/10.1103/PhysRevE.77.036405

[21] Varin, C., Payeur, S., Marceau, V., Fourmaux, S., April, A., Schmidt, B., Fortin, P.-L., Thiré, N., Brabec, T., Légaré, F., Kieffer, J.-C., Piché, M.: Direct Electron Acceleration with Radially Polarized Laser Beams. Applied Sciences **3**(1), 70–93 (2013) https://doi.org/10.3390/app3010070

[22] Wang, P.X., Ho, Y.K., Yuan, X.Q., Kong, Q., Cao, N., Sessler, A.M., Esarey, E., Nishida, Y.: Vacuum electron acceleration by an intense laser. Applied Physics Letters **78**(15), 2253–2255 (2001) https://doi.org/10.1063/1.1359486

[23] Esarey, E., Sprangle, P., Krall, J.: Laser acceleration of electrons in vacuum. Physical Review E **52**(5), 5443–5453 (1995) https://doi.org/10.1103/physreve.52.5443

[24] Stupakov, G.V., Zolotorev, M.S.: Ponderomotive Laser Acceleration and Focusing in Vacuum for Generation of Attosecond Electron Bunches. Physical Review Letters **86**(23), 5274–5277 (2001) https://doi.org/10.1103/physrevlett.86.5274

[25] Singh, P.K., Li, F.Y., Huang, C.K., Moreau, A., Hollinger, R., Junghans, A., Favalli, A., Calvi, C., Wang, S., Wang, Y., Song, H., Rocca, J.J., Reinovsky, R.E., Palaniyappan, S.: Vacuum laser acceleration of super-ponderomotive electrons using relativistic transparency injection. Nature Communications **13** (2022) https://doi.org/10.1038/s41467-021-27691-w

[26] Cheng, L.-H., Yao, Z.-W., Zhang, X.-B., Xue, J.-K.: Net electron energy gain induced by superluminal phase velocity and subluminal group velocity of a laser in a plasma channel. Physics of Plasmas **24**(8), 082114 (2017) https://doi.org/10.1063/1.5000072

[27] Sazegari, V., Mirzaie, M., Shokri, B.: Ponderomotive acceleration of electrons in the interaction of arbitrarily polarized laser pulse with a tenuous plasma. Physics of Plasmas **13**(3), 033102 (2006) https://doi.org/10.1063/1.2178187

[28] MENDONÇA, J.T., SILVA, L.O., BINGHAM, R.: Reflection of an electron beam by a photon mirror. Journal of Plasma Physics **73**(5), 627–634 (2006) https://doi.org/10.1017/s0022377806006064

[29] Robinson, A.P.L.: A critical analysis of the 'ponderomotive snowplow' concept in direct laser acceleration of electrons. Plasma Physics and Controlled Fusion **63**(6), 064003 (2021) https://doi.org/10.1088/1361-6587/abf254

[30] Chong, A., Renninger, W.H., Christodoulides, D.N., Wise, F.W.: Airy–Bessel wave packets as versatile linear light bullets. Nature photonics **4**(2), 103–106 (2010) https://doi.org/10.1038/nphoton.2009.264

[31] Kondakci, H.E., Abouraddy, A.F.: Optical space-time wave packets having arbitrary group velocities in free space. Nature Communications **10**(1), 929 (2019) https://doi.org/10.1038/s41467-019-08735-8

[32] Yessenov, M., Bhaduri, B., Delfyett, P.J., Abouraddy, A.F.: Free-space optical delay line using space-time wave packets. Nature Communications **11**(1), 5782 (2020) https://doi.org/10.1038/s41467-020-19526-x 1910.05616

[33] Vitek, D.N., Adams, D.E., Johnson, A., Tsai, P.S., Backus, S., Durfee, C.G., Kleinfeld, D., Squier, J.A.: Temporally focused femtosecond laser pulses for low numerical aperture micromachining through optically transparent materials. Opt. Express **18**(17), 18086–18094 (2010) https://doi.org/10.1364/OE.18.018086

[34] Vitek, D.N., Block, E., Bellouard, Y., Adams, D.E., Backus, S., Kleinfeld, D., Durfee, C.G., Squier, J.A.: Spatio-temporally focused femtosecond laser pulses for nonreciprocal writing in optically transparent materials. Opt. Express **18**(24), 24673–24678 (2010) https://doi.org/10.1364/OE.18.024673

[35] Durfee, C.G., Greco, M., Block, E., Vitek, D., Squier, J.A.: Intuitive analysis of space-time focusing with double-ABCD calculation. Optics Express **20**(13), 14244 (2012) https://doi.org/10.1364/oe.20.014244

[36] Wilhelm, A.M., Durfee, C.G.: Tilted Snowplow Ponderomotive Electron Acceleration With Spatio-Temporally Shaped Ultrafast Laser Pulses. Frontiers in Physics **7**, 3316 (2019) https://doi.org/10.3389/fphy.2019.00066

[37] Ramsey, D., Franke, P., Simpson, T.T., Froula, D.H., Palastro, J.P.: Vacuum acceleration of electrons in a dynamic laser pulse. Physical Review E **102**(4), 043207 (2020) https://doi.org/10.1103/physreve.102.043207 2007.05430

[38] Froula, D.H., Turnbull, D., Davies, A.S., Kessler, T.J., Haberberger, D., Palastro, J.P., Bahk, S.-W., Begishev, I.A., Boni, R., Bucht, S., Katz, J., Shaw, J.L.: Spatiotemporal control of laser intensity. Nature Photonics **12**(5), 262–265 (2018) https://doi.org/10.1038/s41566-018-0121-8

[39] Kabacinski, A., Oliva, E., Tissandier, F., Gautier, J., Kozlová, M., Goddet, J.-P., Andriyash, I.A., Thaury, C., Zeitoun, P., Sebban, S.: Spatio-temporal couplings for controlling group velocity in longitudinally pumped seeded soft X-ray lasers. Nature Photonics **17**(4), 354–359 (2023) https://doi.org/10.1038/s41566-023-01165-5

[40] Esarey, E., Schroeder, C.B., Leemans, W.P.: Physics of laser-driven plasma-based electron accelerators. Reviews of Modern Physics **81**(3), 1229–1285 (2009) https://doi.org/10.1103/revmodphys.81.1229

[41] Zha, J.J., Qin, Z.H., Yuan, C., Wang, P.X.: High energy positron source driven by laser pulses. Nuclear Instruments and Methods in Physics Research Section

A: Accelerators, Spectrometers, Detectors and Associated Equipment **917**, 43–46 (2019) https://doi.org/10.1016/j.nima.2018.11.117 . a reference for positron acceleration

[42] Zewail, A.H.: 4D Ultrafast Electron Diffraction, Crystallography, and Microscopy. Annual review of physical chemistry **57**(1), 65–103 (2006) https://doi.org/10.1146/annurev.physchem.57.032905.104748

[43] Mora, P., Antonsen, T.M.: Kinetic modeling of intense, short laser pulses propagating in tenuous plasmas. Physics of Plasmas **4**, 217–229 (1997) https://doi.org/10.1063/1.872134

[44] Zhu, G., Howe, J., Durst, M., Zipfel, W., Xu, C.: Simultaneous spatial and temporal focusing of femtosecond pulses. Opt. Express **13**(6), 2153–2159 (2005) https://doi.org/10.1364/OPEX.13.002153

[45] Wang, Y., Wang, S., Rockwood, A., Luther, B.M., Hollinger, R., Curtis, A., Calvi, C., Menoni, C.S., Rocca, J.J.: 085 PW laser operation at 33 Hz and high-contrast ultrahigh-intensity $\lambda = 400$ nm second-harmonic beamline. Optics Letters **42**(19), 3828 (2017) https://doi.org/10.1364/ol.42.003828

[46] Block, E., Thomas, J., Durfee, C., Squier, J.: Integrated single grating compressor for variable pulse front tilt in simultaneously spatially and temporally focused systems. Optics letters **39**(24), 6915–6918 (2014) https://doi.org/10.1364/ol.39.006915

[47] Shen, X., Du, S., Liang, W., Wang, P., Liu, J., Li, R.: Two-step pulse compressor based on asymmetric four-grating compressor for femtosecond petawatt lasers. Applied Physics B **128**(8), 159 (2022) https://doi.org/10.1007/s00340-022-07878-9 2105.04863

[48] Schnell, M., Sävert, A., Uschmann, I., Reuter, M., Nicolai, M., Kämpfer, T., Landgraf, B., Jäckel, O., Jansen, O., Pukhov, A., Kaluza, M.C., Spielmann, C.: Optical control of hard X-ray polarization by electron injection in a laser wakefield accelerator. Nature Communications **4** (2013) https://doi.org/10.1038/ncomms3421 . PFT by misaligning parallelism of gratings - probably not a large PFT, will lead to non-overlapped frequencies at the beamlet waist - can defocus be used to get good overlap?

[49] Zhu, C.-q., Wang, J.-g., Li, Y.-f., Feng, J., Li, D.-z., He, Y.-h., Tan, J.-h., Ma, J.-l., Lu, X., Li, Y.-t., Chen, L.-m.: Optical steering of electron beam in laser plasma accelerators. Optics Express **28**(8), 11609 (2020) https://doi.org/10.1364/oe.380842

[50] Greco, M.J., Block, E., Meier, A.K., Beaman, A., Cooper, S., Iliev, M., Squier, J.A., Durfee, C.G.: Spatial–spectral characterization of focused spatially chirped broadband laser beams. Applied Optics **54**(33), 9818–9822 (2015) https://doi.

org/10.1364/ao.54.009818

[51] Miranda, M., Arnold, C.L., Fordell, T., Silva, F., Alonso, B., Weigand, R., L'Huillier, A., Crespo, H.: Characterization of broadband few-cycle laser pulses with the d-scan technique. Opt. Express20 (17), 18732–18743 (2012)

[52] Wilhelm, A.M., Schmidt, D.D., Adams, D.E., Durfee, C.G.: Multi-mode root preserving ptychographic phase retrieval algorithm for dispersion scan. Optics Express **29**(14), 22080 (2021) https://doi.org/10.1364/oe.426859

[53] Glinec, Y., Faure, J., Guemnie-Tafo, A., Malka, V., Monard, H., Larbre, J.P., De Waele, V., Marignier, J.L., Mostafavi, M.: Absolute calibration for a broad range single shot electron spectrometer. Review of Scientific Instruments **77**(10), 103301 (2006) https://doi.org/10.1063/1.2360988 https://pubs.aip.org/aip/rsi/article-pdf/doi/10.1063/1.2360988/11169366/103301_1_online.pdf

[54] Comby, A., Beaulieu, S., Constant, E., Descamps, D., Petit, S., Mairesse, Y.: Absolute gas density profiling in high-order harmonic generation. Optics Express **26**(5), 6001 (2018) https://doi.org/10.1364/oe.26.006001

[55] Shpilman, Z., Park, J., Nedbailo, R., Hollinger, R., Wang, S., Osovsky, R., Afeyan, B., Rocca, J.J.: Variable magnetic field electron spectrometer to measure hot electrons in the range of 50–460 keV. Review of Scientific Instruments **94**(5), 053303 (2023) https://doi.org/10.1063/5.0142238

[56] Akturk, S., Gu, X., Zeek, E., Trebino, R.: Pulse-front tilt caused by spatial and temporal chirp (1996)